

THE ARIZONA CDFS ENVIRONMENT SURVEY (ACES): A MAGELLAN/IMACS SPECTROSCOPIC SURVEY OF THE CHANDRA DEEP FIELD SOUTH*

MICHAEL C. COOPER^{1,†,2,‡}, RENBIN YAN³, MARK DICKINSON⁴, STÉPHANIE JUNEAU^{2,5}, JENNIFER M. LOTZ⁶, JEFFREY A. NEWMAN⁷, CASEY PAPOVICH⁸, SAMIR SALIM⁹, GREGORY WALTH², BENJAMIN J. WEINER², CHRISTOPHER N. A. WILLMER²

Draft version April 19, 2019

ABSTRACT

We present the Arizona CDFS Environment Survey (ACES), a recently-completed spectroscopic redshift survey of the Chandra Deep Field South (CDFS) conducted using IMACS on the Magellan-Baade telescope. In total, the survey targeted 7277 unique sources down to a limiting magnitude of $R_{AB} = 24.1$, yielding 5080 secure redshifts across the $\sim 30' \times 30'$ extended CDFS region. The ACES dataset delivers a significant increase to both the spatial coverage and the sampling density of the spectroscopic observations in the field. Combined with previously-published, spectroscopic redshifts, ACES now creates a highly-complete survey of the galaxy population at $R < 23$, enabling the local galaxy density (or environment) on relatively small scales (~ 1 Mpc) to be measured at $z < 1$ in one of the most heavily-studied and data-rich fields in the sky. Here, we describe the motivation, design, and implementation of the survey and present a preliminary redshift and environment catalog. In addition, we utilize the ACES spectroscopic redshift catalog to assess the quality of photometric redshifts from both the COMBO-17 and MUSYC imaging surveys of the CDFS.

Subject headings: galaxies: distances and redshifts; catalogs; surveys

1. INTRODUCTION

Building upon the initial X-ray observations of Giaconi et al. (2001, 2002), the Chandra Deep Field South (CDFS, $\alpha = 03^{\text{h}}32^{\text{m}}25^{\text{s}}$, $\delta = -27^{\circ}49^{\text{m}}58^{\text{s}}$) has quickly become one of the most well-studied extragalactic fields in the sky with existing observations among the deepest at a broad range of wavelengths (e.g., Giavalisco et al. 2004; Rix et al. 2004; Lehmer et al. 2005; Quadri et al. 2007; Miller et al. 2008; Padovani et al. 2009; Cardamone et al. 2010; Xue et al. 2011; Damen et al. 2011; Elbaz et al. in prep). In the coming years, this status as one of the very deepest multiwavelength survey fields will be further cemented by the ongoing and upcoming extremely-deep observations with *Spitzer*/IRAC and *HST*/WFC3-IR as part of the Spitzer Extended Deep Survey (SEDS, PI G.

Fazio) and the Cosmic Assembly Near-IR Deep Extragalactic Legacy Survey (CANDELS, Grogin et al. 2011), respectively.

Despite the large commitment of telescope time from both space- and ground-based facilities devoted to imaging the CDFS, spectroscopic observations in the field have generally lagged those in other, comparably-deep extragalactic survey fields. For example, in the Extended Groth Strip, another deep field targeted by the SEDS and CANDELS programs, the DEEP2 and DEEP3 Galaxy Redshift Surveys (Davis et al. 2003, 2007; Cooper et al. 2011a,b, Newman et al. in prep; Cooper et al. in prep; see also Weiner et al. 2006) have created a vast spectroscopic database, achieving an impressive $\sim 60\%$ redshift completeness down to $R_{AB} = 24.1$ across more than 0.2 square degrees and $\gtrsim 40\%$ completeness covering a broader area of ~ 0.5 square degrees down to the same magnitude limit. Similarly, there have been a variety of spectroscopic efforts in the GOODS-N field including the Team Keck Redshift Survey (TKRS, Wirth et al. 2004, see also Cooper et al. 2011a) in addition to the independent work of various groups (e.g., Lowenthal et al. 1997; Phillips et al. 1997; Cohen et al. 2000; Dawson et al. 2001; Cowie et al. 2004; Treu et al. 2005; Reddy et al. 2006; Barger et al. 2008). Together, these datasets provide spectroscopic redshifts for $> 90\%$ of sources down to $z_{\text{F850LP}} = 23.3$ (Barger et al. 2008).

These large spectroscopic surveys add significant scientific utility to the associated imaging datasets, making the photometric constraints much more powerful. For example, spectroscopic redshifts allow critical rest-frame quantities to be derived with increased precision. Furthermore, only through spectroscopy can assorted spectral and dynamical properties (such as the strengths and velocity widths of emission and absorption lines) be measured — in this regard, the spectral databases provided by surveys such as DEEP2, DEEP3, and TKRS are especially powerful due to their uniform spectral range and

* This paper includes data gathered with the 6.5 meter Magellan Telescopes located at Las Campanas Observatory, Chile.

¹ Center for Galaxy Evolution, Department of Physics and Astronomy, University of California, Irvine, 4129 Frederick Reines Hall, Irvine, CA 92697, USA; m.cooper@uci.edu

[†] Hubble Fellow

² Steward Observatory, University of Arizona, 933 N. Cherry Avenue, Tucson, AZ 85721, USA

[‡] Spitzer Fellow

³ Center for Cosmology and Particle Physics, Department of Physics, New York University, 4 Washington Place, New York, NY 10003, USA

⁴ National Optical Astronomy Observatory, 950 North Cherry Avenue, Tucson, AZ 85719

⁵ Laboratoire AIM, CEA/DSM-CNRS-Université Paris Diderot, Irfu/Service d'Astrophysique, CEA-Saclay, Orme des Merisiers, 91191 Gif-sur-Yvette Cedex, France

⁶ Space Telescope Science Institute, 3700 San Martin Drive, Baltimore, MD 21218, USA

⁷ Pittsburgh Particle Physics, Astrophysics, and Cosmology Center (PITT-PACC), Department of Physics and Astronomy, University of Pittsburgh, 3941 O'Hara Street, Pittsburgh, PA 15260, USA

⁸ Department of Physics and Astronomy, Texas A&M University, College Station, TX 77845, USA

⁹ Department of Astronomy, Indiana University, Bloomington, IN 47404, USA

resolution. Finally, only with the combination of high (and relatively uniform) sampling density, spatial coverage across a modestly-sized field (e.g., $\gtrsim 0.05$ square degrees), and moderately high-precision spectroscopic redshifts (i.e., $\sigma_z < 0.01$) can the local galaxy density (or “environment”) be measured across a broad and continuous range of environments (Cooper et al. 2005, 2007).

In contrast to the EGS and GOODS-N fields, the spectroscopic redshift completeness across the extended $30' \times 30'$ area of the CDFS is a modest $\lesssim 25\%$ down to a limiting magnitude of $R_{AB} = 23$ and $\lesssim 20\%$ at $R_{AB} < 24$, despite some significant spectroscopic efforts in the field (e.g., Le Fèvre et al. 2004; Szokoly et al. 2004; Vanzella et al. 2005, 2006, 2008; Mignoli et al. 2005; Ravikumar et al. 2007; Popesso et al. 2009; Balestra et al. 2010; Silverman et al. 2010).⁴ Notably, many of these existing spectroscopic programs have focused their efforts on the smaller GOODS-S region and/or targeted optically-faint, higher-redshift ($z > 1.5$) sources (e.g., Dickinson et al. 2004; Doherty et al. 2005; Roche et al. 2006; Vanzella et al. 2009).

With the goal of creating a highly-complete redshift survey at $z < 1$ in the CDFS, the Arizona CDFS Environment Survey (ACES) utilized the Inamori-Magellan Areal Camera and Spectrograph (IMACS, Dressler et al. 2011) on the Magellan-Baade telescope to collect spectra of more than 7000 unique sources across a $\sim 30' \times 30'$ region centered on the CDFS. In Sections 2 and 3, we describe the design, execution, and reduction of the ACES observations, with a preliminary redshift and environment catalog presented in Sections 4 and 5. Finally, in Section 6, we conclude with a discussion of future work related to ACES. Throughout, we employ a Lambda cold dark matter (Λ CDM) cosmology with $w = -1$, $\Omega_m = 0.3$, $\Omega_\Lambda = 0.7$, and a Hubble parameter of $H_0 = 100 h \text{ km s}^{-1} \text{ Mpc}^{-1}$. All magnitudes are on the AB system (Oke & Gunn 1983), unless otherwise noted.

2. TARGET SELECTION AND SLITMASK DESIGN

The ACES target sample is drawn from the COMBO-17 photometric catalog of Wolf et al. (2004, see also Wolf et al. 2001, 2008). The primary spectroscopic sample is magnitude limited at $R_{AB} < 23$, plus a significant population of fainter sources down to $R_{AB} = 24.1$. Altogether, ACES observations spanned four separate observing seasons (2007B – 2010B), with the details of the target-selection algorithm and slitmask-design parameters varying from year to year. Here, we highlight the critical elements of the composite target population and slitmasks, including any significant variations from mask to mask.

As stated above, the primary target sample for ACES was selected according to an R -band magnitude limit of

⁴ The PRIMUS program (Coil et al. 2011) has collected spectra for a rather large number of sources in a larger area surrounding the CDFS. However, the relatively low resolution ($R = \lambda/\Delta\lambda \sim 30$) of the prism-based spectroscopy limits the utility of the PRIMUS dataset for detailed studies of spectral properties (e.g., emission-line equivalent widths) and small-scale environment (e.g., on group scales).

⁵ To select the galaxy population, all sources classified as “Star” or “WDwarf” in the COMBO-17 photometric catalog of Wolf et al. (2004) are excluded.

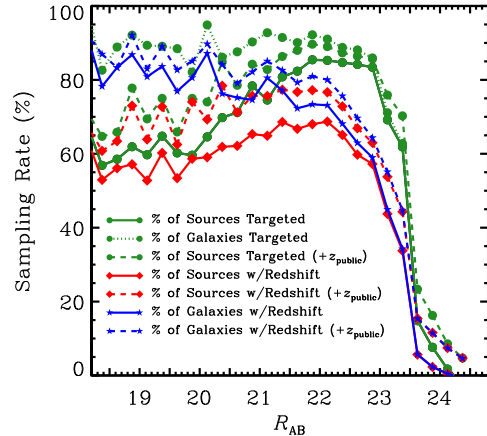


FIG. 1.— The ACES target sampling and redshift success rates as a function of R -band magnitude (green and red solid lines, respectively) across the entire $\sim 30' \times 30'$ COMBO-17/CDFS footprint. The respective sampling rates are defined as the percentage of objects at a given R -band magnitude in the COMBO-17 photometric catalog (including stars) that were observed by ACES [target sampling rate] and yielded a secure ($Q = -1, 3, 4$ – see §4) redshift [redshift sampling rate]. The solid blue line shows the redshift completeness when only considering sources classified as non-stellar in the COMBO-17 catalog.⁵ At bright magnitudes, $R_{AB} < 23$, the ACES sample is highly complete. The corresponding red, green, and blue dashed lines show the associated completeness when accounting for sources with a published spectroscopic redshift in the literature (see §2), and the green dotted line gives the target sampling rate for ACES excluding stellar sources in the same manner as described for the blue lines above.

$R_{AB} < 23$. Selecting in R (versus a redder passband such as I or K) ensures the highest possible signal-to-noise ratio in the continuum of the resulting optical spectra, and thus a high redshift-success rate for the survey. The given magnitude limit was adopted to enable a high level of completeness to be reached across the entire CDFS area. Moreover, at $z \sim 1$, the $R = 23$ limit reaches L^* along the red sequence and 1 magnitude fainter than L^* in the blue cloud population (Willmer et al. 2006), thereby enabling ACES to probe the systems that dominate the galaxy luminosity density and global star-formation rate at $z < 1$. As shown in Figure 1, ACES is highly-complete at $R < 23$, achieving a targeting rate of $\gtrsim 80\%$ across the extended CDFS.

In addition to the main $R < 23$ target sample, we prioritized $70\mu\text{m}$ sources detected as part of the Far-Infrared Deep Extragalactic Legacy (FIDEL) Survey (PI: M. Dickinson), which surveyed the CDFS to extremely deep flux limits at both $24\mu\text{m}$ and $70\mu\text{m}$ with *Spitzer*/MIPS (Magnelli et al. 2009, 2011). In selecting the optical counterparts to the $70\mu\text{m}$ sources, we utilized a fainter magnitude limit of $R = 24.1$, targeting multiple optical sources in cases for which the identity of the optical counterpart was ambiguous. In total, ACES prioritized 529 sources as $70\mu\text{m}$ counterparts, with $\sim 80\%$ of these sources also meeting the $R < 23$ primary magnitude limit for the survey. For the $70\mu\text{m}$ -selected target population, our redshift success rate is quite high ($\sim 80\%$ versus $\sim 70\%$ for the full target population).

As a filler population in the target-selection process, we also included (with a lower selection probability) all sources down to the secondary magnitude limit of $R < 24.1$. These fainter, optically-selected sources comprise

roughly 30% of the total unique target sample (i.e., ~ 2500 sources). The $R = 24.1$ limit was adopted to match that of the DEEP2 Survey and allows the ACES dataset to probe even farther down the galaxy luminosity function at $z < 1$.

To maximize the sampling density of the survey at $0.2 < z < 1$, stellar sources were down-weighted in the target selection process. Stars were identified according to the spectral classification of Wolf et al. (2004), which utilized template SED fits to the 17-band photometry of COMBO-17. All sources classified as “Star” or “WDwarf” by Wolf et al. (2004) were down-weighted in the target selection. This included a total of ~ 1000 sources at $R < 23$. As illustrated in Figure 1, these stellar sources are only a significant contribution to the total R -band number counts at bright ($R < 21.5$) magnitudes; excluding this population of stars from the accounting, ACES targets $> 80\%$ of sources at $R < 23$.

In selecting the ACES spectroscopic targets, we also down-weighted many sources with an existing spectroscopic redshift in the literature. This sample of “public” redshifts was drawn from Le Fèvre et al. (2004), Vanzella et al. (2005, 2006), Mignoli et al. (2005), Ravikumar et al. (2007), Szokoly et al. (2004), Popesso et al. (2009), and Balestra et al. (2010) as well as a small set of proprietary redshifts measured by the DEEP2 Galaxy Redshift Survey using Keck/DEIMOS. In all cases, only secure redshifts were employed. For example, only quality “A” and “B” (not “C”) redshifts were included from Vanzella et al. (2005, 2006); Popesso et al. (2009); Balestra et al. (2010). At $R_{AB} < 24.1$, a total of 2149 unique sources with a spectroscopic redshift were down-weighted in the target selection process, with 1218 of these sources at $R < 23$. A significant number of objects (1288) in this public catalog were observed by ACES; a comparison of the ACES redshift measurements to those previously published is presented in §4. Note that some of these public redshifts (most notably those of Balestra et al. 2010) were not yet published prior to the commencement of ACES, but were included in the target selection process as the survey progressed. Also, the distribution of the existing spectroscopic redshifts on the sky is strongly biased towards the center of the extended CDFS, primarily covering the smaller GOODS-S region (see Fig. 3).

For the 2007B through 2009B observing seasons, slitmasks were designed in pairs, sharing a common position and orientation. By placing two masks at the same location on the sky, objects had multiple chances to be included on a slitmask (and thus observed). Furthermore, we were able to integrate longer on fainter targets by including those sources on both of the masks at a given position, while only including brighter sources on a single mask and thus maximizing the number of sources observed. As discussed in §6, data for objects appearing on multiple slitmasks have yet to be combined; at present, each slitmask is analyzed independently, such that there are a higher number of repeated observations of some objects (especially fainter targets).

The tiling scheme for the 40 IMACS slitmasks was designed to cover the extended $\sim 30' \times 30'$ area of the extended CDFS, with the caveat that the position and orientation of each slitmask was dictated by the availability of suitably bright stars for guiding and dynamic focus-

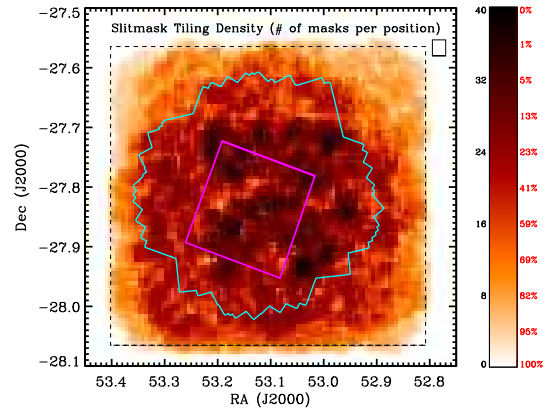


FIG. 2.— The number of Magellan/IMACS slitmasks covering a given spatial location (computed within a box of width $\Delta\alpha = 90''$ and height $\Delta\delta = 96''$) as a function of position within the CDFS. The red values to the right of the color bar show the portion of the $30' \times 30'$ extended CDFS area (demarcated by the black dashed line in the plot) that is covered by greater than the corresponding number of slitmasks. ACES includes a total of 40 slitmasks, with 82% of the field covered by at least 8 slitmasks. Finally, the magenta and cyan outlines indicate the location of the CANDELS *HST*/WFC3-IR and 2-Ms *Chandra*/ACIS-I observations, respectively. Every object in the field has multiple chances to be placed on an ACES slitmask, helping to achieve a high sampling density and minimize any bias against objects in overdense regions on the sky.

ing.⁶ A moderate resolution grism and wide-band (5650–9200Å) filter were employed in the observations (see §3), allowing multiple (2–3) targets to occupy a given spatial position on a slitmask and thereby enable upwards of ~ 400 sources to be observed on a single slitmask. The average number of targets per mask was ~ 350 , with the details of the slitmask design varying slightly from year to year of observing.

For all of the ACES slitmasks, a standard $1''$ slitwidth was employed, with a minimum slitlength of $\sim 7''$ (centered on the target) and a gap of at least $0.5''$ between slits. For a subset of the slitmasks, slits were extended to fill otherwise unoccupied real estate on the slitmask. On every mask, the set of possible targets was restricted to those sources for which the entire spectral range of 5650–9200Å would fall on the detector, given the position and orientation of the mask. The location of the slitmasks on the sky was selected such that the full area of the mask would fall within the CDFS region, leading to a slitmask tiling scheme that more highly samples the central portion of the field. This relative oversampling is a direct product of the large size of the IMACS field-of-view at f2 ($\sim 25' \times 25'$ unvignetted); any IMACS slitmask that falls entirely within the extended CDFS region will overlap the central portion of the CDFS, independent of orientation. As shown in Figure 2, the number of ACES slitmasks at a given position within the CDFS varies significantly from $\gtrsim 30$ at the center of the field to ~ 10 at the edges.

In spite of this spatial variation in the total sampling rate, ACES achieves a relatively uniform spatial sam-

⁶ Note that the Magellan-Baade telescope includes an atmospheric dispersion corrector (ADC) for the f/11 Nasmyth position of IMACS.

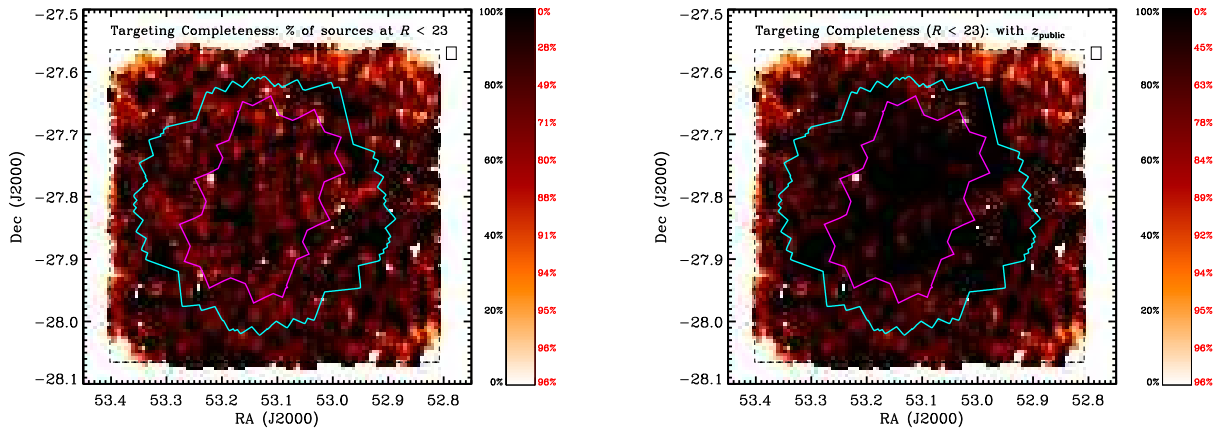


FIG. 3.— The target sampling rate at $R_{AB} < 23$ for the ACES target sample alone (*left*) and for the joint population comprised of the ACES target sample and the set of existing public redshifts detailed in §2 (*right*), computed in a sliding box of width $\Delta\alpha = 64''$ and height $\Delta\delta = 72''$. The size and shape of the box are illustrated in the upper right-hand corner of each plot. The associated color bars give the mapping from color to target completeness (where black and white correspond to 100% and 0% completeness, respectively) and completeness is defined as the percentage of sources in the COMBO-17 imaging catalog with $R_{AB} < 23$ (including stars) targeted by ACES (or ACES plus the set of sources with existing published redshifts). The red values to the right of each color bar show the portion of the $30' \times 30'$ extended CDFS area (demarcated by the black dashed line in each plot) that has a target completeness greater than the corresponding level. Finally, the magenta and cyan outlines indicate the location of the GOODS *HST*/ACS and 2-Ms *Chandra*/ACIS-I observations, respectively. At $R < 23$, the sampling rate is exceptionally high ($\gtrsim 70\%$ from ACES alone) across nearly the entire extended CDFS.

pling rate for the main ($R < 23$) galaxy sample. As evident in Figure 3, ACES targets $\gtrsim 80\%$ of sources at $R < 23$, independent of position within the CDFS. When including spectroscopic observations from the literature, the target sampling is remarkably complete at $R < 23$, with roughly half of the $\sim 30' \times 30'$ CDFS surveyed to $\sim 90\%$ completeness. This relatively high and uniform sampling rate is critical for the ability to measure local environments with the ACES dataset.

3. OBSERVATIONS AND DATA REDUCTION

ACES spectroscopic observations employed the f/2 camera in the Inamori-Magellan Areal Camera and Spectrograph (IMACS) on the Magellan-Baade telescope and were completed across four separate observing seasons (2007B – 2010B) as detailed in Table 1. The instrument set-up included the 200 lines mm^{-1} grism (blaze angle of 15°) in conjunction with the WB5650–9200 wide-band filter, which yields a nominal spectral coverage of 5650–9200Å at a resolution of $R \equiv \lambda/\Delta\lambda \sim 750$ (at 7500Å). Each slitmask was observed for a total integration time of ~ 4500 –7200 sec, divided into (at least) 3–4 individual ~ 1500 –1800 sec integrations (with no dithering performed) to facilitate the rejection of cosmic rays — see Table 1 for details regarding the total integration times. Immediately following each set of science exposures (i.e., without moving the telescope or modifying the instrument configuration), a quartz flat-field frame and comparison arc spectrum (using He, Ar, Ne) were taken to account for instrument flexure and detector fringing.

There are two notable variations in the instrument configuration that occurred in the course of the ACES observations. Between the 2007B (January 2008) and 2008B (November 2008) observing seasons, the IMACS CCDs were upgraded from the original SITE to deep-depletion E2V chips (Dressler et al. 2011). The new CCDs provided much improved quantum efficiency, especially at red wavelengths. In addition to the detector

update, for the initial observing run (in January 2008), the data were collected using the incorrect grism. Instead of the 200 lines mm^{-1} grism, the higher-resolution 300 lines mm^{-1} grism (blaze angle of 17.5°) was installed in IMACS. The resulting spectra from those slitmasks (ACES1–ACES8) are therefore at slightly higher resolution ($R \equiv \lambda/\Delta\lambda \sim 1100$ at 7500Å). Given that the slitmasks multiplex in the spectral (in addition to the spatial) direction and were designed for use with the lower-resolution grism, the spectra for many objects overlap significantly. In addition, for a subset of the objects (primarily those located closer to the edge of the slitmask), part of the 5650–9200Å spectral window was dispersed off of the IMACS detector. In such instances, on the order of 300Å was typically lost at either the blue or red extreme of the spectral window. While the data taken on this first observing run were negatively impacted by the use of the incorrect grism (including a slight reduction in total throughput), redshifts were still able to be measured for many of the targets. In an attempt to maintain the uniformity of the dataset, however, the vast majority of the objects on the ACES1–ACES8 slitmasks (1166 of 1315 objects) were reobserved in subsequent observing seasons.

The IMACS spectroscopic observations were reduced using the COSMOS data reduction pipeline developed at the Carnegie Observatories (Dressler et al. 2011).⁷ For each slitlet, COSMOS yields a flat-fielded and sky-subtracted, two-dimensional spectrum, with wavelength calibration performed by fitting to the arc lamp emission lines. One-dimensional spectra were extracted and redshifts were measured from the reduced spectra using additional software developed as part of the DEEP2 Galaxy Redshift Survey and adapted for use with IMACS as part of ACES and as part of the spectroscopic follow-

⁷ <http://obs.carnegiescience.edu/Code/cosmos>

TABLE 1
 SLITMASK OBSERVATION INFORMATION

Slitmask Name	Observation Date (UT)	α (J2000) ^a	δ (J2000) ^b	P.A. ^c (deg)	N_0 ^d	N_z ^e	Exposure Time ^f
ACES1	2008 Jan 02	03 32 22.000	-27 53 25.00	90	376	160	7200s
ACES2	2009 Jan 02	03 32 22.000	-27 53 25.00	90	313	148	7200s
ACES3	2008 Jan 04	03 32 16.610	-27 43 58.29	90	327	168	7200s
ACES4	2008 Jan 04	03 32 16.610	-27 43 58.29	90	280	36	7200s
ACES7	2008 Jan 03	03 32 33.983	-27 54 00.00	90	339	137	7200s
ACES8	2008 Jan 03	03 32 33.983	-27 54 00.00	90	297	111	7200s
ACES81	2008 Nov 25	03 32 33.750	-27 53 48.58	90	303	170	7200s
ACES82	2008 Nov 25	03 32 33.750	-27 53 48.58	90	348	238	8631s
ACES83	2008 Nov 25	03 32 16.500	-27 54 45.00	90	343	194	7200s
ACES84	2008 Nov 26	03 32 16.500	-27 54 45.00	90	367	249	7200s
ACES85	2008 Nov 26	03 32 40.000	-27 48 30.00	0	359	273	7200s
ACES86	2008 Nov 26	03 32 40.000	-27 48 30.00	0	381	175	7400s
ACES87	2008 Nov 27	03 32 25.690	-27 49 40.00	90	376	202	7200s
ACES88	2008 Nov 27	03 32 25.690	-27 49 40.00	90	378	244	7200s
ACES91	2008 Nov 28	03 32 51.000	-27 47 45.00	0	366	212	7200s
ACES92	2008 Nov 28	03 32 51.000	-27 47 45.00	0	352	193	7200s
ACES93	2008 Nov 27	03 31 57.000	-27 47 45.00	180	364	206	7500s
ACES94	2008 Nov 28	03 31 57.000	-27 47 45.00	180	319	135	7740s
ACES101	2009 Nov 14	03 32 25.690	-27 49 40.00	90	361	172	7200s
ACES102	2009 Nov 15	03 32 25.690	-27 49 40.00	90	337	127	7200s
ACES103	2009 Nov 14	03 32 33.750	-27 53 48.58	90	345	143	9000s
ACES104	2009 Nov 14	03 32 33.750	-27 53 48.58	90	345	188	7200s
ACES105	2009 Nov 16	03 32 16.500	-27 54 45.00	90	339	132	7200s
ACES106	2009 Nov 16	03 32 16.500	-27 54 45.00	90	340	168	4800s
ACES107	2009 Nov 15	03 32 40.000	-27 48 30.00	0	348	116	6850s
ACES108	2009 Nov 15	03 32 40.000	-27 48 30.00	0	356	191	7200s
ACES109	2009 Nov 16	03 31 57.000	-27 47 45.00	180	340	127	5400s
ACES110	2009 Nov 16	03 31 57.000	-27 47 45.00	180	340	161	4500s
ACES201	2010 Dec 09	03 32 30.500	-27 49 50.00	0	370	216	4500s
ACES202	2010 Dec 10	03 32 33.750	-27 53 48.58	90	360	210	5400s
ACES203	2010 Dec 10	03 31 57.000	-27 47 45.00	180	362	243	6900s
ACES204	2010 Dec 09	03 32 40.000	-27 48 30.00	0	364	213	4500s
ACES205	2010 Dec 09	03 32 16.500	-27 54 45.00	90	352	111	4500s
ACES206	2010 Dec 09	03 32 51.000	-27 47 45.00	0	364	200	4500s
ACES207	2010 Dec 11	03 32 30.000	-27 48 00.00	90	368	227	5400s
ACES208	2010 Dec 11	03 32 25.690	-27 49 40.00	90	359	227	5400s
ACES209	2010 Dec 10	03 32 25.000	-27 46 15.00	90	361	242	5400s
ACES210	2010 Dec 10	03 32 25.690	-27 52 35.00	90	349	153	5100s
ACES211	2010 Dec 11	03 32 10.000	-27 48 00.00	0	360	210	5040s
ACES212	2010 Dec 11	03 32 54.000	-27 49 40.00	0	355	100	5400s

NOTE. — Details of the ACES Magellan/IMACS slitmasks.

^aRight ascension (in hr mn sc) of the slitmask center.

^bDeclination (in deg min sec) of the slitmask center.

^cPosition angle of the slitmask (E of N).

^dNumber of targets on slitmask.

^eNumber of secure ($Q = -1, 3, 4$) redshifts measured on slitmask.

^fTotal exposure time for slitmask (in seconds).

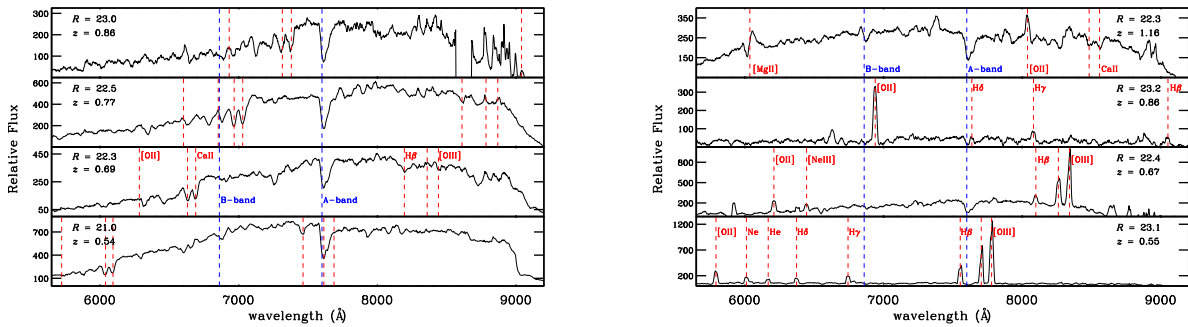


FIG. 4.— Example ACES one-dimensional spectra of red and/or passive galaxies (*left*) and star-forming/active galaxies (*right*). The location of prominent spectral features as well as the A- and B-band telluric features are indicated by the red and blue dashed vertical lines, respectively. Note that the spectra have been smoothed (weighted by the inverse variance) using a kernel of 15 pixels (or 30Å) in width.

up of the Red-Sequence Cluster Survey (RCS, Gladders & Yee 2005; z RCS, Yan et al. in prep). Example spectra

for objects spanning a broad range of galaxy type and apparent magnitude are shown in Figure 4. All spectra

were visually inspected, with a quality code (Q) assigned corresponding to the accuracy of the redshift value — $Q = -1, 3, 4$ denote secure redshifts, with $Q = -1$ corresponding to stellar sources and $Q = 3, 4$ denoting secure galaxy redshifts (see Table 2). As discussed in §4.2, $Q = 3$ and $Q = 4$ redshifts are estimated to be $>90\%$ and $>95\%$ reliable, respectively. Quality codes of $Q = 1, 2$ are assigned to observations that yield no useful redshift information ($Q = 1$) or may possibly yield redshift information after further analysis or re-reduction of the data ($Q = 2$). For detailed descriptions of the reduction pipeline, redshift measurement code, and quality assignment process refer to Wirth et al. (2004), Davis et al. (2007), and Newman et al. (in preparation).

4. REDSHIFT CATALOG

A preliminary ACES redshift catalog is presented in Table 2, a subset of which is listed herein. The entirety of Table 2 appears in the electronic version of the Journal. Note that a redshift is only included when classified as being secure, ($Q = -1, 3, 4$). The total number of secure redshifts in the sample is 5080 out of 7277 total, unique targets. The redshift distribution for this sample, as shown in Figure 5, is biased towards $z < 1$, with a tail out to higher redshift.

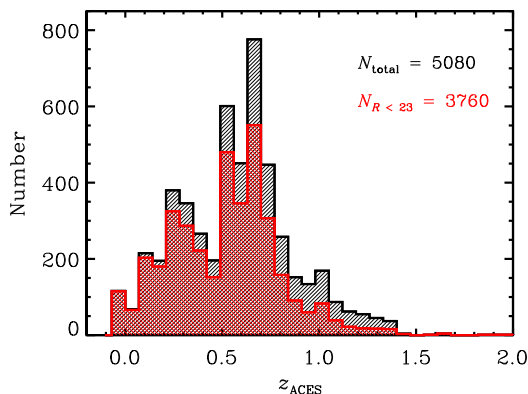


FIG. 5.— The distribution of the 5080 unique, secure ($Q = -1, 3, 4$) redshifts measured by ACES (black histogram). The red histogram shows the distribution for the main ($R < 23$) target sample. The main sample is biased towards $z < 0.8$, with a tail to higher redshift.

The ACES catalog has a high number of repeated observations (as discussed in §2). These independent observations provide a direct means for determining the precision of the redshift measurements. As shown in Figure 6, we find a scatter of $\sigma_z \sim 75 \text{ km s}^{-1}$ within the ACES sample when comparing repeat observations of a sizable sample of secure redshifts. The scatter is found to be independent of the redshift quality (i.e., $Q = 3$ versus $Q = 4$). While the precision of the ACES redshifts is poorer than that of surveys such as DEEP2 and DEEP3, it is adequate for characterizing local environments (Cooper et al. 2005) as well as identifying and measuring the velocity dispersions of galaxy groups.

4.1. Comparison to Photometric Redshift Samples

The ACES spectroscopic sample provides an excellent dataset with which to test the precision of the COMBO-17 photometric redshift measurements. The COMBO-

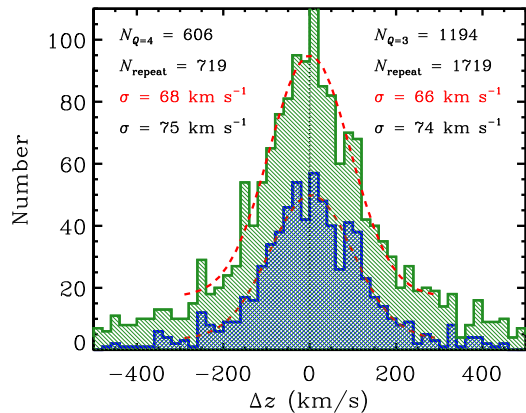


FIG. 6.— The distribution of velocity differences computed from repeated observations, where both observations of a given galaxy yielded a $Q = 4$ (blue histogram) or $Q = 3$ redshift (green histogram). A total of 606 and 1194 unique sources comprise the two distributions separately. The dispersion as given by a Gaussian fit to the distribution (red dashed line) and by the square root of the second moment of the distribution are reported in red and black font (or top and bottom numbers), respectively. A total of 2438 pairs of observations comprise the two distributions, with a dispersion of $\sigma \sim 75 \text{ km s}^{-1}$ independent of redshift quality.

17 photo- z estimates are based on 17-band photometry spanning 3500\AA to 9300\AA . While their accuracy at higher redshift is impacted significantly by the lack of near-IR observations, the COMBO-17 photometric redshifts are very robust at $z < 1$. Based on a comparison to a relatively small (<1000 , primarily at $z < 0.3$) sample of spectroscopic redshifts, Wolf et al. (2004) found a $1\text{-}\sigma$ error of $\sigma_z/(1+z) < 0.01$, with a less than 1% catastrophic failure rate (where failure is defined to be $\Delta z/(1+z) > 0.05$).

In Figure 7, we directly compare the COMBO-17 photometric redshifts to the ACES spectroscopic redshifts for all sources with a secure ($Q = -1, 3, 4$) redshift. The deficiency of objects at $z \sim 0.9$ results largely from the inability of ACES to resolve the [O II] doublet. That is, the ACES spectrum of an emission-line galaxy at $z \sim 0.9$ would yield an unresolved [O II] emission doublet at $\sim 7100\text{\AA}$, while $H\beta$ and [O III] would be redward of our spectral window ($>9200\text{\AA}$). We are unable to easily distinguish this single emission line from $H\alpha$ (i.e., a galaxy at $z \sim 0.08$), as at that redshift $H\beta$ and [O III] would be blueward of our spectral window ($<5650\text{\AA}$). As a result, many objects at $z \sim 0.9$ are classified as $Q = 2$. Using broad-band color info, we hope to recover these objects in the future (e.g., Kirby et al. 2007).

Within the ACES dataset alone, there are 4769 objects with a secure galaxy redshift (i.e., $Q = 3, 4$) and a photometric redshift in the catalog of Wolf et al. (2004). For this set of objects, the COMBO-17 photometric redshifts exhibit a dispersion of $\sigma_z/(1+z) \sim 0.015$ (with $3\text{-}\sigma$ outliers removed) and a catastrophic failure rate (again taken to be $\Delta z/(1+z) > 0.05$) of $>10\%$. As highlighted by Wolf et al. (2004), however, the COMBO-17 photometric redshifts degrade in quality for increasingly fainter galaxies, and the ACES sample extends to $R = 24.1$. For bright objects ($R \leq 22$), the dispersion relative to the ACES spectroscopic redshifts is $\sigma_z/(1+z) \sim 0.012$ (again with $3\text{-}\sigma$ outliers removed), with a catastrophic failure rate of 6%. The precision is slightly poorer at fainter magnitudes ($22 < R < 23$),

increasing to $\sigma_z/(1+z) \sim 0.014$, while at the faintest magnitudes probed by ACES, the scatter between the COMBO-17 photo- z values and our spectroscopic redshifts increases to $\sigma_z/(1+z) \sim 0.022$ (for $R \geq 23$). For the main $R < 23$ sample, the catastrophic failure rate ($|\Delta z|/(1+z) > 0.05$) is 8%.

These trends with apparent magnitude and redshift are evident in Figure 8, which shows the dependence of the photometric redshift error ($\sigma_z/(1+z)$) and the catastrophic failure rate on R -band magnitude, redshift, and observed $R-I$ color based on a comparison of the ACES spectroscopic redshift and COMBO-17 photometric redshift catalogs. At faint magnitudes ($R > 23$) and at higher redshift ($z > 1$), the photometric-redshift errors and failure rates for COMBO-17 increase significantly. However, we find no significant correlation between the quality of the photometric redshifts and apparent $R-I$ color, suggesting that there is little dependence on the spectral-type or star-formation history of a galaxy.

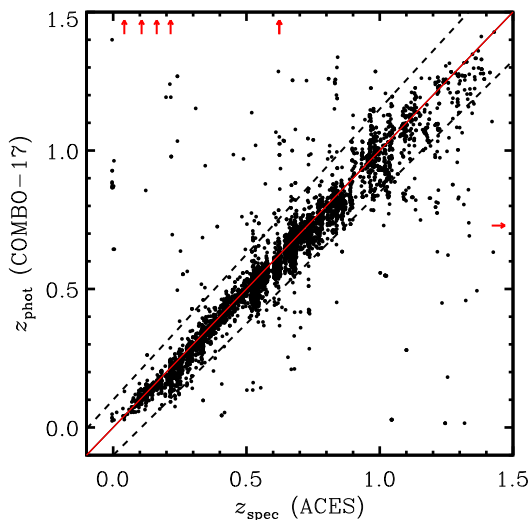


FIG. 7.— A comparison of the spectroscopic redshifts from ACES to the photometric redshifts of COMBO-17 (Wolf et al. 2004). In general, the agreement is quite good, with a dispersion of $\sigma_z/(1+z) \sim 0.015$ (with $3\text{-}\sigma$ outliers removed) for the galaxy ($Q = 3,4$) sample. The red vertical arrows indicate sources for which the photometric redshift value is greater than $z = 1.5$, in conflict with the spectroscopic value, which is indicated by the position of the arrow (and vice versa for the red horizontal arrow). The dashed black lines correspond to a nominal catastrophic failure level of $|\Delta z|/(1+z) = 0.05$.

As highlighted earlier, the degradation in photo- z quality with redshift is in part due to the lack of near-IR photometry in the multi-band imaging of COMBO-17. In contrast, the photometric redshifts from the Multiwavelength Survey by Yale-Chile (MUSYC, Gawiser et al. 2006), as computed by Cardamone et al. (2010), include broad-band optical and near-IR (JHK) imaging in addition to photometry in 18 medium-bands from Subaru. As shown in Figure 8, the MUSYC photometric redshifts exhibit much smaller scatter in relation to the ACES spectroscopic redshift sample, with $\sigma_z/(1+z) \sim 0.005$ across the full magnitude and redshift range probed. In addition, the catastrophic failure rate for the MUSYC sample is roughly a factor of 2 lower than that found for the COMBO-17 photometric redshift catalog.

4.2. Comparison to Spectroscopic Redshift Samples

Matching our catalog to previously-published spectroscopic redshifts in the field (e.g., Le Fèvre et al. 2004; Vanzella et al. 2005, 2006; Balestra et al. 2010, see §2), we find 1288 of our targets have a redshift published as part of these existing datasets. For 941 of these 1288 objects, we measure a secure redshift from our IMACS spectroscopy. The agreement between the ACES redshifts and those in the literature is generally good. We find a median offset of $|\Delta z| \sim 240 \text{ km s}^{-1}$ when comparing to the “public” redshift catalog detailed in §2. For the small set of significant outliers (the 44 objects with $|\Delta z| > 3000 \text{ km s}^{-1}$), the ACES spectra were re-examined to confirm that the validity of the ACES redshifts. Some of these could be the result of mismatching between the ACES catalog and the public databases, but the majority are the result of line misidentification (e.g., confusing $H\alpha$ with $[OII]$) or some other failure in redshift identification (see Figure 9).

The significant overlap between the ACES sample and the set of existing redshifts in the literature also provides a means to conservatively estimate the reliability of the ACES redshifts. Taking the previously-published values to be the true redshift for each galaxy, we measure the catastrophic failure rate ($|\Delta z| = |z_{\text{public}} - z_{\text{ACES}}| > 1000 \text{ km s}^{-1}$) for the $Q = 3$ and $Q = 4$ ACES redshifts. For the 351 sources with $Q = 3$ and 586 source with $Q = 4$ redshifts in the ACES catalog, we find failure rates of 13% and 6%, respectively. As shown in Figure 9, some of the previously-published redshifts are clearly in error, thus these confidence values are conservative estimates. Comparing within the ACES sample alone, we find that 6% and 2% of sources with repeated observations (both yielding $Q = 3$ and $Q = 4$ redshifts — see Fig. 6) have redshifts measurements that disagree at greater than 500 km s^{-1} .

The new redshifts presented here should significantly enhance studies of galaxy evolution and cosmology in the CDFS. Our sample expands upon previous spectroscopic work in the field, significantly increasing the size of the existing redshift database. Furthermore, our observations broaden the area covered, extending beyond the GOODS-S HST/ACS footprint, allowing us to target a greater number of relatively rare sources. In particular, we specifically targeted *Spitzer*/MIPS $70\mu\text{m}$ sources, including those observed by previous spectroscopic efforts in the field. Within the FIDEL Survey’s *Spitzer*/MIPS $70\mu\text{m}$ photometric catalog for GOODS-S, which covers an area of roughly $10' \times 10'$, there are only 44 sources detected at $> 2.5 \text{ mJy}$ (Magnelli et al. 2011). The relatively small number of these sources puts a premium on spectroscopic follow-up, including those located outside of the GOODS-S area. The FIDEL Survey covers a broader region surrounding the GOODS-S area, actually extending significantly beyond the ACES footprint in most directions when combined with existing *Spitzer*/MIPS observations. In total, $\gtrsim 500$ sources are detected (down to $S_{70\mu\text{m}} \sim 0.5 \text{ mJy}$) at $70\mu\text{m}$ within the COMBO-17 footprint as part of the FIDEL survey (requiring a $3\text{-}\sigma$ detection at both $24\mu\text{m}$ and $70\mu\text{m}$). As highlighted in §2, ACES targets 529 sources as potential optical counterparts to these sources (i.e., within $3''$ of a $70\mu\text{m}$ source).

The $70\mu\text{m}$ observations conducted as part of the FI-

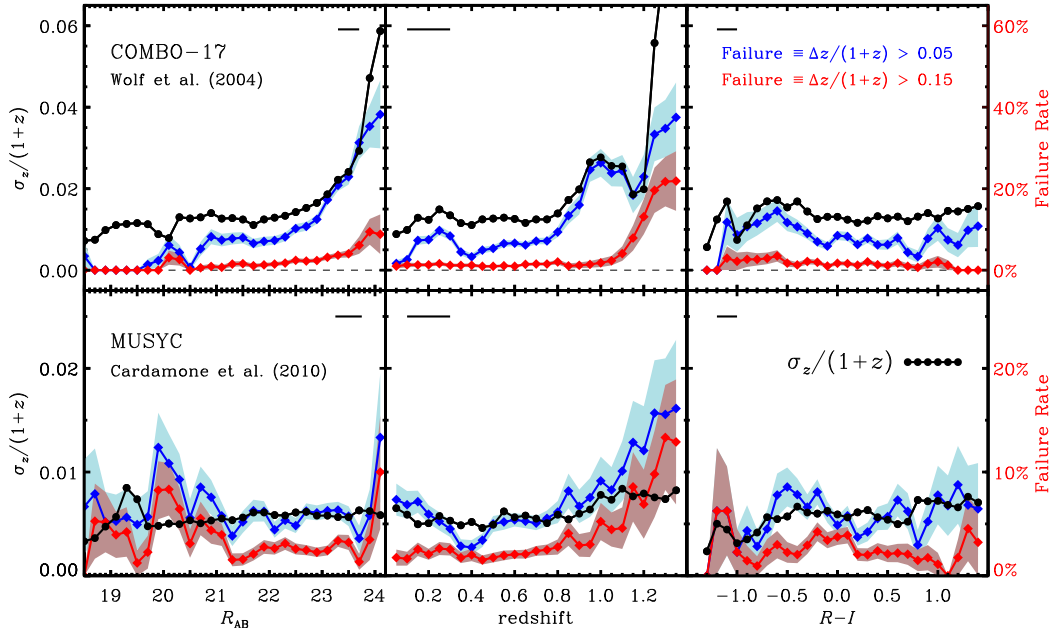


FIG. 8.— The dependence of the photometric redshift error ($\sigma_z/(1+z)$) and the catastrophic failure rate on R -band magnitude (left), redshift (middle), and observed $R-I$ color (right) for the COMBO-17 (top) and MUSYC (bottom) photometric redshift catalogs. The errors (black points) and failure rates (blue and red diamonds) are computed using sliding boxes with widths given by the black dashes in the upper corner of each plot, while the light blue and red shaded regions denote the 1σ uncertainty on the respective failure rates, as given by binomial statistics. In all cases, the dispersions ($\sigma_z/(1+z)$) are computed with 3σ outliers removed. In determining the redshift and color dependences, only objects with $R < 23$ are included. For COMBO-17, the photo- z errors and failure rates increase significantly at fainter magnitudes ($R > 23$) and higher redshift ($z > 1$), while the trends are much weaker for the MUSYC photometric redshifts.

DEL Survey are the deepest in the sky, allowing significant numbers of star-forming galaxies and active galactic nuclei to be detected out to intermediate redshift at rest-frame wavelengths that are dramatically less impacted by aromatic and silicate emission than those normally probed by *Spitzer*/MIPS $24\mu\text{m}$ observations. With accompanying redshift information from spectroscopic follow-up such as presented here, these deep far-infrared data provide a unique constraint on the cosmic star-formation history at intermediate redshift (e.g., Magnelli et al. 2009).

5. ENVIRONMENT MEASURES

By extending beyond the GOODS-S footprint (i.e., the area primarily targeted by previous spectroscopic efforts in the field), ACES substantially expands the area over which galaxy overdensity (or “environment”) can be measured in the CDFS. The finite area of sky covered by a survey introduces geometric distortions — or edge effects — which bias environment measures near borders (or holes) in the survey field, generally leading to an underestimate of the local overdensity (Cooper et al. 2005, 2006). To minimize the impact of these edge effects on studies of environment, galaxies near the edge of the survey field (e.g., within a projected distance of $1-2 h^{-1}$ comoving Mpc of an edge) are often excluded from any analysis. As such, the ACES dataset, which spans a considerably larger region than previous spectroscopic samples (and with a much more spatially uniform targeting rate, see Fig. 3 and Fig. 10), now allows the environment of galaxies at intermediate redshift to be accurately

computed across nearly the entire $\sim 30' \times 30'$ area of the CDFS, thereby enabling unique analyses of small-scale clustering in one of the most well-studied extragalactic fields in the sky.

For each galaxy in the ACES redshift catalog (see Table 2), we estimate the local galaxy overdensity, or “environment”, using measurements of the projected third-nearest-neighbor surface density (Σ_3) about each galaxy, where the surface density depends on the projected distance to the third-nearest neighbor, $D_{p,3}$, as $\Sigma_3 = 3/(\pi D_{p,3}^2)$. Over quasi-linear regimes, the mass density and galaxy density should simply differ by a factor of the galaxy bias (Kaiser 1987). In computing Σ_3 , only objects within a velocity window of $\pm 1250 \text{ km s}^{-1}$ are counted, to exclude foreground and background galaxies along the line-of-sight. To explore any dependencies on the choice of N in this N^{th} -nearest-neighbor approach to measuring environment, we also compute overdensities based on the distance to the fourth- and fifth-nearest-neighbor (see Table 3).

When estimating the local environment within a survey dataset, each surface density measurement must be corrected according to the redshift and spatial dependence of the survey’s sampling rate. To minimize the variation in the spatial component of the ACES sampling rate, we select the $R < 23$ galaxy population as the tracer population by which the local galaxy density is defined — note that this is done both with and without the public redshifts included and environment measures based on each tracer population are provided in Table

TABLE 2
ACES REDSHIFT CATALOG

Object ID ^a	α^b (J2000)	δ^c (J2000)	R_{AB}^d	Mask ^e	Slit ^f	MJD ^g	flag _{70μm}} ^h	z^i	z_{helio}^j	Q^k	z_{other}^ℓ	Ref ^m
122	53.038740	-28.064493	22.54	ACES105	152	55150.9	0	0.38687	0.38686	4
215	53.053105	-28.063773	21.05	ACES106	163	55151.7	0	1
15629	52.978946	-27.943812	23.15	ACES102	085	55150.6	0	0.74274	0.74272	3

NOTE. — Table 2 is presented in its entirety in the electronic edition of the Journal. A portion is shown here for guidance regarding its form and content.

^aObject identification number (SEQ) in R -band catalog of Wolf et al. (2004).

^bRight ascension in decimal degrees from Wolf et al. (2004).

^cDeclination in decimal degrees from Wolf et al. (2004).

^d R -band magnitude in AB system from Wolf et al. (2004).

^eName of IMACS slitmask on which object was observed.

^fNumber of slit on IMACS slitmask corresponding to object.

^gModified Julian Date of observation.

^hTargeting flag: 0 = main R -band selected target; 1 = *Spitzer*/*MIPS* 70 μ m target

ⁱRedshift derived from observed spectrum.

^jHeliocentric-frame redshift.

^kRedshift quality code (star = -1; \sim 90% confidence = 3; \sim 95% confidence = 4; unknown = 1, 2).

^lAlternate redshift from literature.

^mSource of alternate redshift: (1) DEEP2/DEIMOS; (2) Le Fèvre et al. (2004); (3) Vanzella et al. (2005); (4) Vanzella et al. (2006); (5) Mignoli et al. (2005); (6) Ravikumar et al. (2007); (7) Szokoly et al. (2004); (8) Popesso et al. (2009); Balestra et al. (2010)

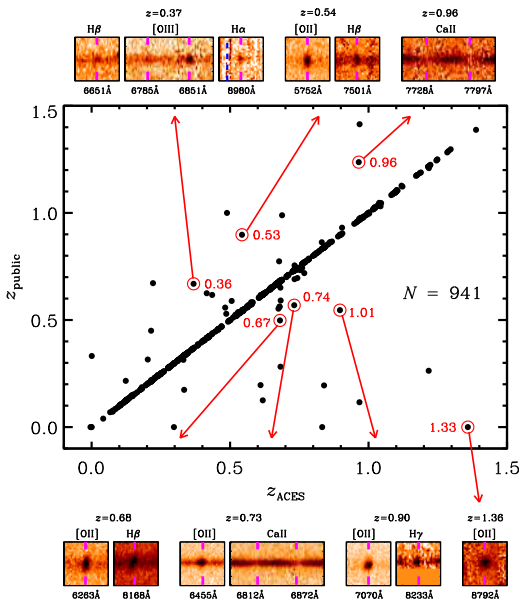


FIG. 9.— For the sample of 941 objects with a secure redshift in ACES (i.e., $Q = -1, 3, \text{ or } 4$) and also a secure measurement in the literature, we plot a comparison of the two spectroscopic redshift measurements. The agreement is quite good, with only 47 objects having redshift measurements that disagree at $|\Delta z| > 3000 \text{ km s}^{-1}$. For 7 of these outliers, we show cut-outs from the Magellan/IMACS two-dimensional spectra, illustrating the spectral features that confirm the ACES redshift. In each case, the COMBO-17 photometric redshift (given in red font within the plot) agrees quite well with the ACES spectroscopic redshift. Refer to §4 for details regarding the set of “public” redshift measurements.

3.⁸ While selecting only those objects that meet this bright magnitude limit decreases the sampling density of the tracer population (relative to the full ACES dataset), the main $R < 23$ galaxy sample has a well-defined and relatively uniform spatial selection rate (see Figure 3 and Fig. 10). Using this highly-complete tracer population,

⁸ See Cooper et al. (2009, 2010b) for additional discussion regarding the selection of tracer populations in the measurement of environments.

we measure the surface density, Σ_3 (as described above), about all galaxies in the ACES redshift catalog, independent of apparent magnitude. With or without the public redshifts included, the typical projected distance to the third-nearest neighbor, $D_{p,3}$, is $\sim 1 h^{-1} \text{ Mpc}$ at $0.2 < z < 0.8$.

To correct for the redshift dependence of the ACES sampling rate, each surface density is divided by the median Σ_3 for all galaxies within a window $\Delta z = 0.03$ centered on the redshift of each galaxy; this converts the Σ_3 values into measures of overdensity relative to the median density (given by the notation $1 + \delta_3$ herein) and effectively accounts for the redshift variations in the selection rate (Cooper et al. 2005, 2006, 2008a). We restrict our environment catalog to the redshift range $0.2 < z < 0.8$, avoiding the low- and high-redshift tails of the ACES redshift distribution (see Fig. 5) where the variations in the survey selection rate are the greatest.

Finally, to enable the effects of edges and holes in the survey geometry to be minimized, we measure the distance to the nearest survey boundary. We determine the survey area and corresponding edges according to the 2-dimensional survey completeness map ($w(\alpha, \delta)$, see Fig. 10) and the photometric bad-pixel mask, which provides information about the location of bright stars (i.e., undersampled regions) in the field. We define all regions of sky with $w(\alpha, \delta) < 0.3$ averaged over scales of $\gtrsim 30''$ to be unobserved and reject all significant regions of sky ($\gtrsim 30''$ in scale) that are incomplete in the COMBO-17 R -band photometric catalog. Areas of incompleteness on scales smaller than $30''$ are comparable to the typical angular separation of galaxies targeted by ACES and thus cause a negligible perturbation to the measured densities. To minimize the impact of edges on the data sample, we recommend all analyses using these environment values to exclude any galaxy within $1 h^{-1}$ comoving Mpc of an edge or hole; such a cut greatly reduces the portion of the dataset contaminated by edge effects (Cooper et al. 2005).

In Figure 11, we show the distribution of overdensities, $\log_{10}(1 + \delta_3)$, for 3057 galaxies with a secure redshift at

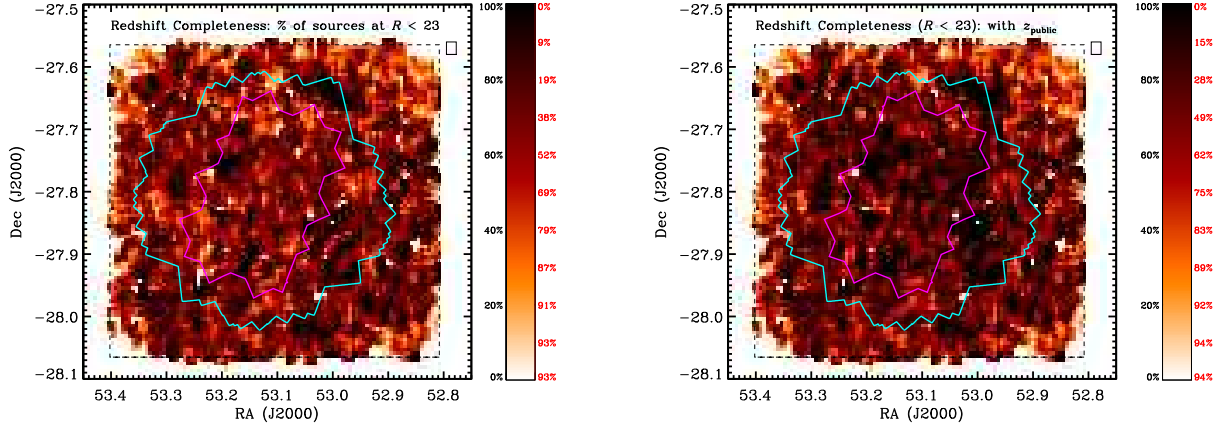


FIG. 10.— The redshift completeness at $R_{\text{AB}} < 23$ for the ACES sample alone (*left*) and for the joint population comprised by ACES and the set of existing public redshifts detailed in §2 (*right*), computed in a sliding box of width $\Delta\alpha = 64''$ and height $\Delta\delta = 72''$. The size and shape of the box are illustrated in the upper right-hand corner of each plot. The associated color bars give the mapping from color to redshift completeness (where black and white correspond to 100% and 0% completeness, respectively) and completeness is defined as the percentage of sources in the COMBO-17 imaging catalog with $R_{\text{AB}} < 23$ (including stars) for which ACES (or ACES plus the set of sources with existing published redshifts) measured a secure redshift (i.e., $Q = -1, 3, 4$). The red values to the right of each color bar show the portion of the $30' \times 30'$ extended CDFS area (demarcated by the black dashed line in each plot) that has a redshift completeness greater than the corresponding level. Finally, the magenta and cyan outlines denote the location of the GOODS *HST*/ACS and 2-Ms *Chandra*/ACIS-I observations, respectively. At $R < 23$, the redshift completeness is high ($\gtrsim 50\%$ from ACES alone) across nearly the entire extended CDFS.

$0.2 < z < 0.8$ in either the ACES redshift catalog or the set of existing public redshifts detailed in §2. Here, we exclude all galaxies within $1 h^{-1}$ comoving Mpc of a survey edge and utilize the environment measures computed with a tracer population comprised of all galaxies at $R < 23$ (using both ACES and “public” secure redshifts). In addition, Figure 11 shows the distribution of environments for those galaxies identified as members of X-ray groups by Finoguenov et al. (2011). Group members are selected within a cylinder with a radius of $0.75 h^{-1}$ Mpc and length of 2000 km s^{-1} , centered on the location of the extended X-ray emission for all groups with $M_{200} > 5 \cdot 10^{12} M_{\odot}$ as given by Finoguenov et al. (2011), where M_{200} is the total gravitational mass (assuming $h = 0.7$) within a radius where the average density is 200 times the critical density (e.g., Finoguenov et al. 2001). Several of the X-ray groups are coincident with known overdensities in the CDFS (e.g., Gilli et al. 2003; Adami et al. 2005; Trevese et al. 2007; Salimbeni et al. 2009), and we find that the group members are preferentially found to have higher values of $\log_{10}(1 + \delta_3)$, thereby providing an independent check of the environment measures presented here.

6. SUMMARY AND FUTURE WORK

We present a spectroscopic survey of the Chandra Deep Field South (CDFS), conducted using Magellan/IMACS and aptly named the Arizona CDFS Environment Survey (ACES). The survey dataset includes 7277 unique spectroscopic targets, yielding 5080 secure redshifts, within the extended CDFS region. We describe in detail the design and implementation of the survey and present preliminary redshift and environment catalogs.

While this work marks a significant increase in both the spatial coverage and the sampling density of the spectroscopic observations in the CDFS, there remains much

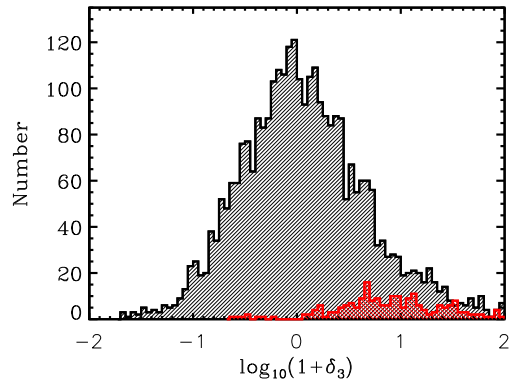


FIG. 11.— The distribution of overdensity measures for all sources with a secure redshift at $0.2 < z < 0.8$ in the joint population comprised of the ACES redshift catalog and the set of existing public redshifts detailed in §2. The red histogram shows the environment distribution for the 210 galaxies identified as group members using the X-ray group catalog of Finoguenov et al. (2011). There is good agreement between the group and environment catalogs.

analysis of the ACES data to be completed in the future. In particular, work is presently underway to produce a relative throughput correction for the spectra, using observations of F stars that were targeted on many of the IMACS slitmasks. The F stars were observed with the same instrumental set-up as the science targets (i.e., same slitwidth, slitlength, etc.) and were included on multiple slitmasks, such that the spectra fell on each of the 8 IMACS CCDs, allowing chip-to-chip variations in the throughput to be estimated.

As discussed in §2, fainter targets ($R \gtrsim 22.5$) were observed on multiple (~ 2 – 4) slitmasks, with the goal of accumulating longer integration times. In the future,

TABLE 3
ACES ENVIRONMENT CATALOG

Object ID ^a	z^b	Ref ^c	D_{edge}^d	ACES only tracer			ACES + z_{public} tracer		
				$\log(1 + \delta_3)^e$	$\log(1 + \delta_4)^f$	$\log(1 + \delta_5)^g$	$\log(1 + \delta_3)^e$	$\log(1 + \delta_4)^f$	$\log(1 + \delta_5)^g$
121	0.3164	0	0.077	-0.930	-0.768	-0.679	-0.975	-0.831	-0.731
122	0.3869	0	0.055	-0.128	0.028	0.018	-0.169	-0.050	-0.041
253	0.7689	0	0.125	-0.489	-0.313	-0.250	-0.542	-0.360	-0.305
263	0.6023	0	0.081	-1.601	-1.434	-1.416	-1.617	-1.478	-1.371

NOTE. — Table 3 is presented in its entirety in the electronic edition of the Journal. A portion is shown here for guidance regarding its form and content. Readers are reminded that galaxies located near a survey edge (e.g., within $\sim 1 h^{-1}$ comoving Mpc) should be excluded from analyses, since the associated environment measures are contaminated by edge effects (see §5).

^aObject identification number (SEQ) in R -band catalog of Wolf et al. (2004).

^bRedshift (in the heliocentric frame).

^cSource of redshift: (0) this work; (1) DEEP2/DEIMOS; (2) Le Fèvre et al. (2004); (3) Vanzella et al. (2005); (4) Vanzella et al. (2006); (5) Mignoli et al. (2005); (6) Ravikumar et al. (2007); (7) Szokoly et al. (2004); (8) Balestra et al. (2010)

^dDistance from nearest survey edge (h^{-1} comoving Mpc).

^eOverdensity as given by the third-nearest-neighbor surface density.

^fOverdensity as given by the fourth-nearest-neighbor surface density.

^gOverdensity as given by the fifth-nearest-neighbor surface density.

these data spanning different slitmasks will be combined, which will likely improve the survey's redshift success rate at fainter magnitudes. In parallel to this work, efforts to improve the spectral reduction procedures are currently underway, which should likewise improve the redshift completeness at all magnitudes. Likewise, future work will include extracting spectra and measuring redshifts for serendipitous detections of objects, an effort that could be helped greatly by the addition of data from different slitmasks. The completion of this ongoing work is expected to coincide with a final data release, including updated redshift and environment catalogs as well as all of the reduced IMACS spectra. Finally, analysis is underway to utilize the ACES data to study the correlations between star-formation history, morphology, and environment at $z < 1$, using the rich multiwavelength data in the CDFS and the increased sample size to improve upon previous efforts (e.g., Elbaz et al. 2007; Capak et al. 2007; Cooper et al. 2008b, 2010a).

This work is based in part on observations made with the Spitzer Space Telescope, which is operated by the Jet Propulsion Laboratory, California Institute of Tech-

nology under a contract with NASA. Support for this work was provided by NASA through the Spitzer Space Telescope Fellowship Program. MCC acknowledges support provided by NASA through Hubble Fellowship grant #HF-51269.01-A, awarded by the Space Telescope Science Institute, which is operated by the Association of Universities for Research in Astronomy, Inc., for NASA, under contract NAS 5-26555. MCC also acknowledges support from the Southern California Center for Galaxy Evolution, a multi-campus research program funded by the University of California Office of Research. This work was also supported in part by NSF grant AST-0806732 and by NASA through an award issued by JPL/Caltech as part of the FIDEL Spitzer Legacy science program. We thank the DEEP2 Galaxy Redshift Survey team for providing access to their Keck/DEIMOS observations of the CDFS. MCC thanks John Mulchaey, Alexis Finoguenov, and Dave Wilman for helpful discussions throughout much of the project and also thanks the entire Las Campanas Observatory staff for their help in the acquisition of the ACES Magellan/IMACS data. Finally, MCC thanks Mike Boylan-Kolchin for helpful discussions in preparing this work.

Facilities: Magellan:Baade (IMACS)

REFERENCES

- Adami, C. et al. 2005, *A&A*, 443, 805
 Balestra, I. et al. 2010, *A&A*, 512, A12+
 Barger, A. J., Cowie, L. L., & Wang, W. 2008, *ApJ*, 689, 687
 Capak, P. et al. 2007, *ApJS*, 172, 284
 Cardamone, C. N. et al. 2010, *ApJS*, 189, 270
 Cohen, J. G., Hogg, D. W., Blandford, R., Cowie, L. L., Hu, E., Songaila, A., Shopbell, P., & Richberg, K. 2000, *ApJ*, 538, 29
 Coil, A. L. et al. 2011, *ApJ*, 741, 8
 Cooper, M. C., Gallazzi, A., Newman, J. A., & Yan, R. 2010a, *MNRAS*, 402, 1942
 Cooper, M. C., Newman, J. A., Madgwick, D. S., Gerke, B. F., Yan, R., & Davis, M. 2005, *ApJ*, 634, 833
 Cooper, M. C., Newman, J. A., & Yan, R. 2009, *ApJ*, 704, 687
 Cooper, M. C., Tremonti, C. A., Newman, J. A., & Zabludoff, A. I. 2008a, *MNRAS*, 390, 245
 Cooper, M. C. et al. 2006, *MNRAS*, 370, 198
 —. 2007, *MNRAS*, 376, 1445
 —. 2008b, *MNRAS*, 383, 1058
 —. 2010b, *MNRAS*, 409, 337
 —. 2011a, *ApJS*, 193, 14
 —. 2011b, ArXiv e-prints
 Cowie, L. L., Barger, A. J., Hu, E. M., Capak, P., & Songaila, A. 2004, *AJ*, 127, 3137
 Damen, M. et al. 2011, *ApJ*, 727, 1
 Davis, M. et al. 2003, in *Society of Photo-Optical Instrumentation Engineers (SPIE) Conference Series*, Vol. 4834, *Society of Photo-Optical Instrumentation Engineers (SPIE) Conference Series*, ed. P. Guhathakurta, 161–172
 Davis, M. et al. 2007, *ApJ*, 660, L1
 Dawson, S., Stern, D., Bunker, A. J., Spinrad, H., & Dey, A. 2001, *AJ*, 122, 598
 Dickinson, M. et al. 2004, *ApJ*, 600, L99
 Doherty, M., Bunker, A. J., Ellis, R. S., & McCarthy, P. J. 2005, *MNRAS*, 361, 525
 Dressler, A. et al. 2011, *PASP*, 123, 288
 Elbaz, D. et al. 2007, *A&A*, 468, 33
 Finoguenov, A., Reiprich, T. H., & Böhringer, H. 2001, *A&A*, 368, 749
 Gawiser, E. et al. 2006, *ApJS*, 162, 1
 Giacomini, R. et al. 2001, *ApJ*, 551, 624

- . 2002, *ApJS*, 139, 369
Giavalisco, M. et al. 2004, *ApJ*, 600, L93
Gilli, R. et al. 2003, *ApJ*, 592, 721
Gladders, M. D. & Yee, H. K. C. 2005, *ApJS*, 157, 1
Grogin, N. A. et al. 2011, *ArXiv e-prints*
Kaiser, N. 1987, *MNRAS*, 227, 1
Kirby, E. N., Guhathakurta, P., Faber, S. M., Koo, D. C., Weiner, B. J., & Cooper, M. C. 2007, *ApJ*, 660, 62
Le Fèvre, O. et al. 2004, *A&A*, 428, 1043
Lehmer, B. D. et al. 2005, *ApJS*, 161, 21
Lowenthal, J. D. et al. 1997, *ApJ*, 481, 673
Magnelli, B., Elbaz, D., Chary, R. R., Dickinson, M., Le Borgne, D., Frayer, D. T., & Willmer, C. N. A. 2009, *A&A*, 496, 57
—. 2011, *A&A*, 528, A35+
Mignoli, M. et al. 2005, *A&A*, 437, 883
Miller, N. A., Fomalont, E. B., Kellermann, K. I., Mainieri, V., Norman, C., Padovani, P., Rosati, P., & Tozzi, P. 2008, *ApJS*, 179, 114
Oke, J. B. & Gunn, J. E. 1983, *ApJ*, 266, 713
Padovani, P., Mainieri, V., Tozzi, P., Kellermann, K. I., Fomalont, E. B., Miller, N., Rosati, P., & Shaver, P. 2009, *ApJ*, 694, 235
Phillips, A. C., Guzman, R., Gallego, J., Koo, D. C., Lowenthal, J. D., Vogt, N. P., Faber, S. M., & Illingworth, G. D. 1997, *ApJ*, 489, 543
Popesso, P. et al. 2009, *A&A*, 494, 443
Quadri, R. et al. 2007, *AJ*, 134, 1103
Ravikumar, C. D. et al. 2007, *A&A*, 465, 1099
Reddy, N. A., Steidel, C. C., Erb, D. K., Shapley, A. E., & Pettini, M. 2006, *ApJ*, 653, 1004
Rix, H.-W. et al. 2004, *ApJS*, 152, 163
Roche, N. D., Dunlop, J., Caputi, K. I., McLure, R., Willott, C. J., & Crampton, D. 2006, *MNRAS*, 370, 74
Salimbeni, S. et al. 2009, *A&A*, 501, 865
Silverman, J. D. et al. 2010, *ApJS*, 191, 124
Szokoly, G. P. et al. 2004, *ApJS*, 155, 271
Treu, T. et al. 2005, *ApJ*, 633, 174
Trevese, D., Castellano, M., Fontana, A., & Giallongo, E. 2007, *A&A*, 463, 853
Vanzella, E. et al. 2005, *A&A*, 434, 53
—. 2006, *A&A*, 454, 423
—. 2008, *A&A*, 478, 83
—. 2009, *ApJ*, 695, 1163
Weiner, B. J. et al. 2006, *ApJ*, 653, 1049
Willmer, C. N. A. et al. 2006, *ApJ*, 647, 853
Wirth, G. D. et al. 2004, *AJ*, 127, 3121
Wolf, C., Dye, S., Kleinheinrich, M., Meisenheimer, K., Rix, H.-W., & Wisotzki, L. 2001, *A&A*, 377, 442
Wolf, C., Hildebrandt, H., Taylor, E. N., & Meisenheimer, K. 2008, *A&A*, 492, 933
Wolf, C. et al. 2004, *A&A*, 421, 913
Xue, Y. Q. et al. 2011, *ApJS*, 195, 10